Journal of
Synchrotron
Radiation

ISSN 1600-5775

Received 20 June 2014
Accepted 31 October 2014

Tuning the phase transition of ZnO thin films through lithography: an integrated bottom-up and top-down processing

Luca Malfatti,[a] Alessandra Pinna,[a] Stefano Enzo,[b] Paolo Falcaro,[c] Benedetta Marmiroli[d] and Plinio Innocenzi[a]*

[a]Laboratorio di Scienza dei Materiali e Nanotecnologie, CR-INSTM, Università di Sassari, Palazzo Pou Salit, Piazza Duomo 6, 07041 Alghero (SS), Italy, [b]Dipartimento di Chimica e Farmacia, Università di Sassari, Local INSTM Unit, Via Vienna 2, 07100 Sassari, Italy, [c]Division of Materials Science and Engineering, CSIRO, Private Bag 33, Clayton South MDC, Victoria 3169, Australia, and [d]Institute of Inorganic Chemistry, Graz University of Technology, Stremayrgasse 9/IV, 8010 Graz, Austria. *E-mail: plinio@uniss.it

An innovative approach towards the physico-chemical tailoring of zinc oxide thin films is reported. The films have been deposited by liquid phase using the sol–gel method and then exposed to hard X-rays, provided by a synchrotron storage ring, for lithography. The use of surfactant and chelating agents in the sol allows easy-to-pattern films made by an organic–inorganic matrix to be deposited. The exposure to hard X-rays strongly affects the nucleation and growth of crystalline ZnO, triggering the formation of two intermediate phases before obtaining a wurtzite-like structure. At the same time, X-ray lithography allows for a fast patterning of the coatings enabling microfabrication for sensing and arrays technology.

© 2015 International Union of Crystallography

Keywords: zinc oxide; thin film; sol–gel; lithography; bottom-up/top-down.

1. Introduction

The electrical and optical properties of zinc oxide have been extensively studied for potential applications in electronic, optoelectronic, photovoltaic, information technology and sensing (Özgür *et al.*, 2005). Several synthetic methods have already been explored to produce pure ZnO films, including sputtering (Tominaga *et al.*, 2002), chemical vapour deposition (CVD) and aerosol-assisted chemical vapour deposition (AACVD) (Naghavi *et al.*, 2000; O'Brien *et al.*, 2010), pulsed laser deposition (Krunks & Mellikov, 1995), spray pyrolysis (Natsume & Sakata, 2002) and the sol–gel process (Farley *et al.*, 2004; Mandalapu *et al.*, 2006). The latter, in particular, is a cheap and versatile synthetic method that allows inorganic and hybrid organic–inorganic thin and thick layers to be produced at room temperature and pressure. After deposition, the films are usually annealed at high temperatures for increasing the oxide polycondensation and, in some cases, inducing crystallization. The sol–gel method has recently been used to obtain ZnO thin layers which remained amorphous up to temperatures of 623 K (O'Brien *et al.*, 2010). The crystalline structure of ZnO films is of paramount importance because the long-range organization at the atomic level of the inorganic matrix is at the basis of the functional properties, such as the electronic band gap. ZnO crystals show two main atomic organizations, that have hexagonal (wurtzite-type) and cubic (zinc-blende-type) symmetry; however, an easy tuning of the ZnO crystalline structure would open new perspectives in the design of thin coatings made by semiconductor oxides, achieving a fine control of the physical–chemical properties over a wide range of applications. Moreover, the possibility of microfabricating ZnO films is of particular interest for the development of functional devices, such as fluorescent microarrays for bio-detection or piezoelectric microdevices, based on the optical and electrical properties of the inorganic oxide (Hu *et al.*, 2011; Cho *et al.*, 2007).

Recently, the sol–gel route has been used in combination with several patterning processes, such as micro-moulding, dip-pen lithography, UV and X-ray lithography, to obtain a combination between the so-called bottom-up and top-down techniques (Innocenzi *et al.*, 2004, 2012). In fact, while the sol–gel chemistry allows for material design starting from its chemical components, an integrated processing provides micro- down to nano-fabrication of the coatings. Besides patterning, some lithographic processes, and in particular deep X-ray lithography (DXRL), are also able to induce chemical modifications in the matrix. In previous years, we have pioneered the use of DXRL as a tool for patterning sol–gel films and inducing at the same time chemical modifications in the exposed areas. This approach has been at first applied to mesoporous organized sol–gel silica films, and then used for a wide variety of sol–gel-based coatings (Falcaro *et al.*, 2008,

2009). Hard X-ray exposure, in fact, is responsible for the formation of radicals, mainly due to the presence of residual water or –OH groups in the as-deposited films. The radicals trigger the polycondensation of the inorganic matrix and degrade the organic groups or moieties that are present in the films after deposition (Pinna *et al.*, 2012; Innocenzi *et al.*, 2011). Recently, exposure to hard X-rays has been exploited for the fabrication of patterns and the formation of nanoparticles in the film matrix. This approach has allowed microarrays made by porous films containing gold and silver nanoparticles to be formed (Innocenzi *et al.*, 2004; Malfatti *et al.*, 2010, 2011). Moreover, we have discovered the possibility of inducing crystallization of oxides, such as cerium oxide nanoparticles, in preformed mesoporous titania films through impregnation with a suitable sol and subsequent exposure to hard X-rays (Pinna *et al.*, 2013). This method has allowed an unprecedented mesopores filling to be obtained that could not be achieved by thermal treatment, with the possibility of producing a pattern of impregnated areas.

In this work, we have used a combination of sol–gel synthesis and DXRL to process ZnO thin films. The chemistry has been carefully designed so that, immediately after deposition, the films behave like efficient resists for lithography. At the same time, the changes induced by hard X-rays into the soft matrix have produced phase transitions which are controlled by the processing conditions.

2. Experimental

2.1. Chemicals

Zinc acetate dihydrate [$Zn(CH_3COO)_2 \cdot 2H_2O$, Aldrich >99.5%], ethyl acetoacetate ($CH_3COCH_2COOC_2H_5$, Aldrich >99%), Pluronic F127 (PEO_{106}-PPO_{70}-PEO_{106}, Aldrich), 2-propanol (Carlo Erba 99.7%), ethanol (Fluka >99.8% EtOH) and 1,2-ethanediol (ethylene glycol; Sigma-Aldrich 99.8%) were used as received without further purification; bidistilled water (H_2O) was employed in the synthesis. p-Type boron-doped silicon wafers were employed as the substrates for film deposition.

2.2. Sol preparation

The precursor sol was prepared by adding 2.2 g of zinc acetate dihydrate and 1.4 g of ethyl acetoacetate into a mixture of 12 g 2-propanol and 2 g Pluronic F127. 10.5 g of water were then added to the precursor sol and left under stirring for 15 min. The sol was deposited by spin-coating on silicon wafers at 6000 r.p.m. for 40 s.

2.3. Materials characterization

Fourier-transform infrared (FTIR) measurements were performed using a Vertex 70 Bruker spectrometer in the 400–4000 cm^{-1} range by averaging 2500 scans with a resolution of 4 cm^{-1} on films deposited on a silicon wafer; silicon was used as background.

The baseline of each spectrum was corrected using a concave rubber-band function with one iteration (*OPUS7* software).

A Wollam-α spectroscopic ellipsometer with fixed-angle geometry was used for thickness and refractive index measurements of thin films deposited on silicon substrates. The thickness was estimated by fitting the experimental data with a Cauchy model for transparent films on Si substrates.

A Bruker M4 Tornado X-ray fluorescence spectrometer with a 100× objective was used to observe the Zn and Si elements content over an area of 0.6 mm × 0.6 mm of patterned films. The samples were washed with ethanol before measuring, to remove the unreacted precursors sol from the unexposed regions. The maps were recorded under vacuum using an X-ray tube with Rh anode at 600 μA and 50 kV with Al 12.5 filter and with a spot size of 4 μm.

The formation of zinc oxide crystallites inside the thin films was detected by a Raman microscope. A Bruker Senterra confocal Raman microscope working with a laser excitation wavelength of 532 nm at 25 mW of nominal power and a resolution of 9 cm^{-1} was used for Raman spectroscopy analysis; the baseline was fit by using a concave rubber-band function with three iterations.

X-ray diffraction (XRD) patterns of zinc oxide thin films were collected using a Bruker D8 Discover diffractometer in grazing-incidence geometry using a Cu $K\alpha$ line (λ = 1.54056 Å); the X-ray generator worked at a power of 40 kV and 40 mA. The patterns were recorded in 2θ ranging from 10 to 100° with a step size of 0.02° and a scan speed of 0.5 s by a repetition mode for 12 h, until maximization of the signal-to-noise ratio was achieved. The XRD patterns were analyzed with *MAUD* software according to the Rietveld method (Lutterotti *et al.*, 1999).

2.4. X-ray lithography

The as-prepared films were directly exposed to hard X-ray radiation using the DXRL beamline at the Elettra synchrotron facility (Trieste, Italy). The storage ring worked at 2 GeV. The samples were mounted on top of a water-cooled stainless steel plate (scanner), which was continuously moving the sample in front of the beam to allow for a homogeneous exposure of areas larger than the beam size; the scanner rate was set to 20 mm s^{-1}. At the exposure plane (position of the sample) the beam size was 115.5 mm × 10.6 mm. The films were irradiated with different doses (energy per unit area at the sample surface) by changing the exposure time (18, 36, 72, 144 and 288 s). The energy per unit area is equal to the exposure time multiplied by the X-ray power per unit area hitting the sample, P = 2.472 W cm^{-2}. The films were exposed to doses corresponding to 45, 89, 178, 356 and 712 J cm^{-2}. For testing the effect of hard X-rays on ZnO crystallization, the films were directly exposed to the X-ray beam without using a lithographic mask. After patterning, the films were treated for 2 h at 200°C, 250°C and 300°C in order to control the crystalline transition and grain dimension of ZnO. The films were placed directly in the oven at selected temperatures, without

using a thermal ramp. A not-exposed sample was also annealed as a reference. For patterning evaluation, a mask containing test patterns of different size, shape and geometry (5–500 μm) was then used to produce patterns on the films that were exposed to the X-ray beam. The mask contained a 20 μm-thick gold absorber and a titanium transparent membrane of thickness 2.2 μm. After exposure, the samples were developed by immersion for 20 s in a mixture of 10 cm^3 ethanol and 5 cm^3 ethylene glycol, so that the unexposed regions of the coating were dissolved. The developed samples were then dried under a nitrogen flow.

3. Results and discussion

The film's composition has been optimized to allow for microfabrication through X-ray lithography; in particular, two specific reactants have been added to the sol used for film deposition: ethyl acetoacetate and Pluronic F127. The first compound is a chelating agent that stabilizes the formation of metal oxide 'clusters' and, at the same time, inhibits crystallization of the zinc oxide precursors (Seisenbaeva & Kessler, 2014). The delayed formation of ZnO crystals provides a good optical quality of the coatings after deposition. The second reactant is a non-ionic tri-block copolymer, which is particularly sensitive to X-ray exposure (Costacurta *et al.*, 2011); the addition of Pluronic F127 to the films enhances the contrast between exposed and unexposed regions providing a better patterning (Falcaro *et al.*, 2009).

Fig. 1(*a*) shows the FTIR absorption spectra in the 3050–2650 cm^{-1} range of the ZnO samples which have been exposed to different X-ray doses. In this wavenumber range, the vibrations due to CH_2 stretching of the Pluronic F127 surfactant can be used to monitor the response of the as-deposited films after exposure at increasing doses. The FTIR band decreases in intensity as a function of the exposure dose indicating the degradation of the surfactant molecules induced by X-rays; no evidence of increased polymerization of the block copolymer is observed, in accordance with previous studies on X-ray-induced modifications of block-copolymer thin films (Innocenzi *et al.*, 2010*a*). The degradation, calculated as the change of the absorption area, shows a strong increase at the lower doses up to 356 J cm^{-2} where around 50% of Pluronic has been removed by the effect of X-rays (Fig. 1*b*). The exposure to highly energetic X-ray photons produces a large amount of free radicals from residual water and –OH groups in the sample. Free radicals are responsible for the degradation of the organic molecules and, at the same time, induce densification of the inorganic matrix *via* hydrolysis/condensation reactions. The trend of the degradation curve mirrors the response of the material to radiation; at lower doses, when more hydroxyls and water are available in the film, the percentage degradation is high; after 50% of Pluronic has been removed, the amount of hydroxyls and water present in the film is reduced, and a further increase of the dose, from 356 to 712 J cm^{-2}, produces only 4% of relative degradation.

Fig. 2 shows the FTIR absorption spectra in the 1200–1030 cm^{-1} range of the as-deposited ZnO film upon exposure

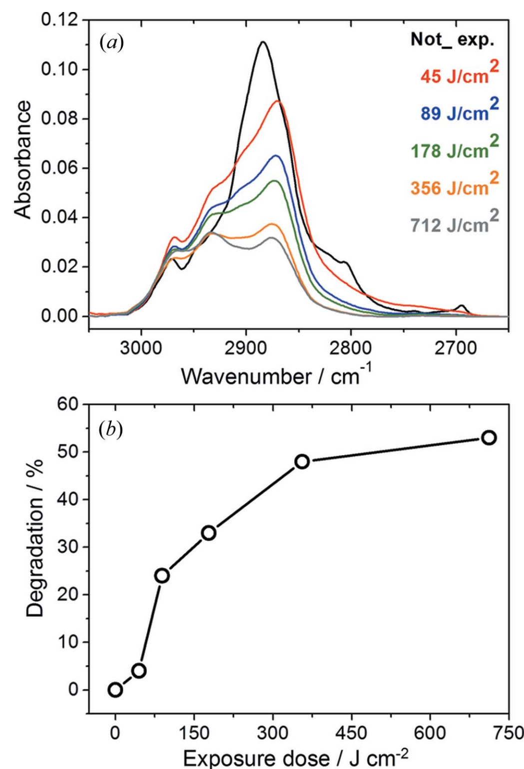

Figure 1
(*a*) FTIR absorption spectra in the 3050–2650 cm^{-1} range of the ZnO samples exposed to different X-ray doses. (*b*) Degradation (%) as a function of exposure dose calculated as the change of the absorption area of the spectra in (*a*). The line is a guide for the eyes.

to different X-ray doses. This wavenumber interval is characteristic of the C—O—C stretching signals (around 1200–1000 cm^{-1}) with the appearance of a typical triplet of intense overlapped bands at 1060 [ν_s(COC) + ρ_s(CH_2)], 1111 [ν_s(COC) or ν_{as}(COC)] and 1150 [ν(CC) − ν_{as} (COC)] cm^{-1} due to the block copolymer. The band decreases in intensity with the increase of the exposure dose, in accordance with the CH_2 stretching signals of Pluronic F127 in Fig. 1, because of the effect of X-rays, and it also shows a significant change in shape (Innocenzi *et al.*, 2010*a*). In the as-deposited sample the spectrum is formed by three intense overlapped bands, which represent the typical signature of crystalline Pluronic

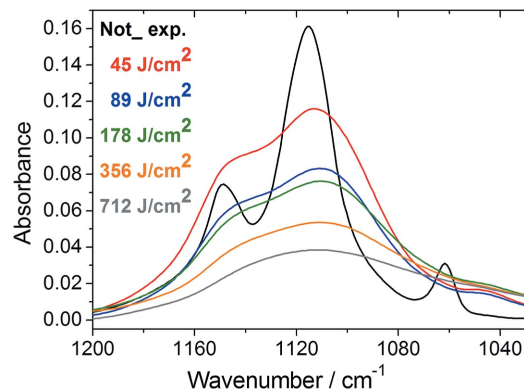

Figure 2
FTIR absorption spectra in the 1200–1030 cm^{-1} range of the as-deposited ZnO films upon exposure to increasing X-ray doses.

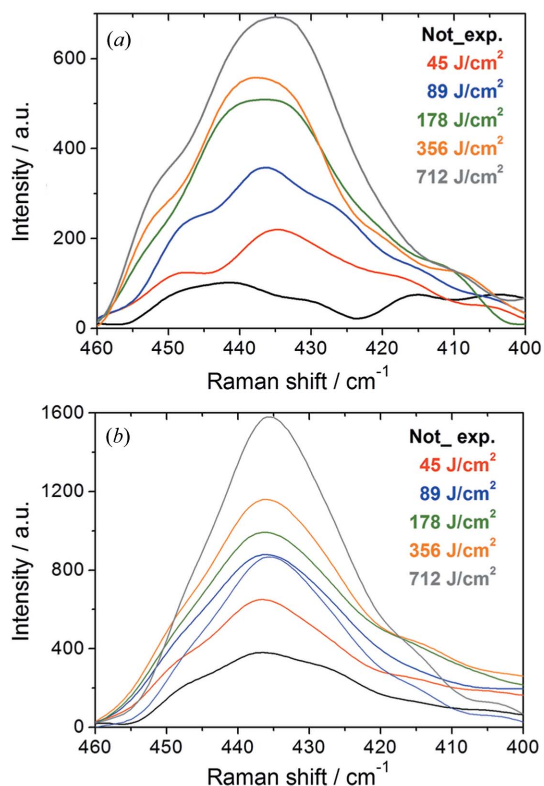

Figure 3
(a) Raman spectra in the 460–400 cm^{-1} range of as-deposited films as a function of the exposure dose. (b) Raman spectra in the 460–400 cm^{-1} range of films annealed at 300°C as a function of the exposure dose.

(Innocenzi *et al.*, 2010*b*). This structure is already lost after exposure to the lowest dose, indicating that the surfactant not only degrades, but quickly undergoes a change into an amorphous phase. X-ray irradiation, therefore, induces both amorphization and degradation of the copolymer in the films; the degradation is obtained through organic bond breaking of the block copolymers so that an increasing amount of by-products, such as carbonyl groups, are observed with increasing doses (see Figure S1 of the supporting information).[1]

The formation of the zinc oxide structure upon X-ray exposure has been followed by Raman spectroscopy; Fig. 3(a) shows the Raman spectra in the 460–400 cm^{-1} range as a function of the dose (the same spectra in a larger wavenumber range are available; see Fig. S2 of the supporting information). The band which peaks around 435 cm^{-1} is attributed to the E_2^{high} Raman mode of the oxygen vibrations in ZnO (Cuscó *et al.*, 2007). This band is characterized by a strong asymmetry attributed to the lattice disorder and the anharmonic phonon–phonon interactions. E_2^{high} goes through significant changes with the increase of exposure dose; the band increases in intensity and decreases the asymmetry, which is due to a reduction of defects associated with the condensation of ZnO and formation of the ZnO crystal lattice. The low intensity of the band exposed at 45 J cm^{-2} indicates that the sample is largely amorphous while the detection of a structured Raman band at higher exposition doses can be associated with the formation of a crystalline lattice, as confirmed by XRD patterns (see below). The spectra, however, do not have a well defined shape even at the highest dose, indicating an incomplete crystallization and defects in the structure. Fig. 3(b) shows the Raman spectra of the same samples after heating at 300°C; the bands in the 460–400 cm^{-1} range show a higher symmetry if compared with untreated films; however, its intensity increases with the exposure dose, suggesting a higher extent of crystalline domains in the exposed samples.

The changes in thickness and refractive index of the samples as a function of the exposure dose have been measured by spectroscopy ellipsometry and are shown in Fig. 4. The films decrease in thickness and increase in refractive index with the increase of the dose, as a result of the densification of the ZnO films induced by the X-rays. The thickness change follows a very similar trend with respect to Pluronic F127 in Fig. 1(b), suggesting a direct correlation between the effect of X-ray dose and densification due to removal of the organic species and condensation of ZnO. The refractive index follows instead a different path with an initial decrease and an increase after 178 J cm^{-2} dose; the first effect is due to the removal of surfactant while the second one is due to the ZnO concentration and crystallization.

The ZnO crystallization under thermal treatment has been studied as a function of the X-ray exposure. Fig. 5 shows the X-ray diffraction pattern of four samples exposed at four increasing X-ray doses (as-deposited, 89, 178 and 356 J cm^{-2}) and treated up to 300°C. Before heating, the not-exposed film [Fig. 5(a), green line] shows a pattern formed by different contributions of the sol precursors; in particular, the presence of crystalline residual zinc acetate dihydrate and crystalline Pluronic F127 can be identified and a tentative peak attribution can be given on the basis of previous studies (Guo *et al.*, 2003; Lee *et al.*, 2011; Mikó *et al.*, 2012). In the ranges between

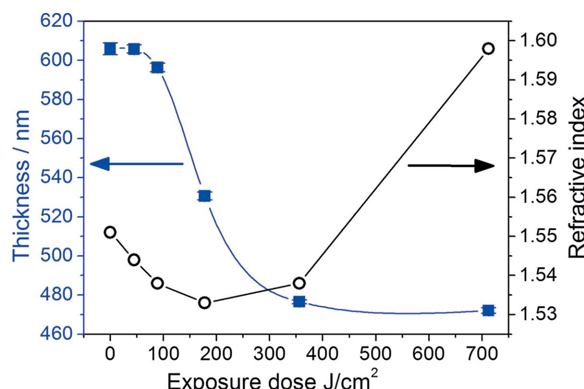

Figure 4
Thickness and refractive index of the samples as a function of the exposure dose, as measured by spectroscopy ellipsometry. The lines are a guide for the eyes.

[1] Supporting information for this paper is available from the IUCr electronic archives (Reference: CO5056). FTIR absorption spectra in the 1800–1675 cm^{-1} range of the as-deposited ZnO films upon exposure to increasing X-ray doses (Figure S1); Raman spectra in the 1200–80 cm^{-1} range of as-deposited films as a function of the exposure dose (Figure S2); XRD patterns at increasing X-ray doses for films annealed at 200°C in the 35–99° and 40–53° 2θ range (Figure S3); optical images of a patterned film before and after thermal treatment at 300°C (Figure S4).

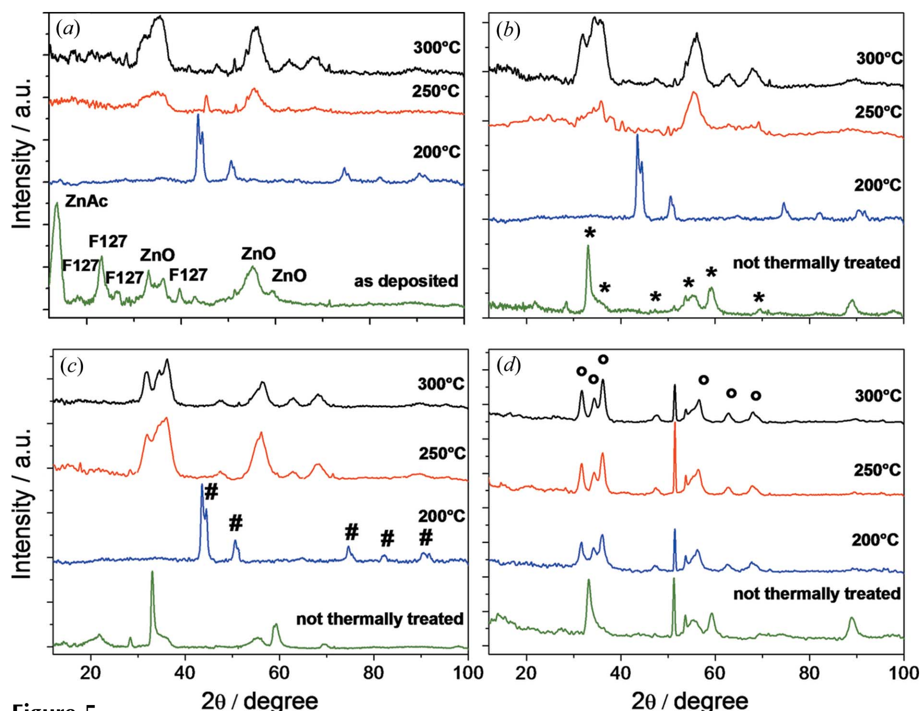

Figure 5
XRD patterns at increasing heating temperatures for films exposed at different X-ray doses: (*a*) not exposed; (*b*) 89 J cm^{-2}; (*c*) 178 J cm^{-2} and (*d*) 356 J cm^{-2}. The asterisks (*) indicate the ZnO* crystalline phase (PDF #21-1486), the hash marks (#) indicate the intermediate f.c.c. crystalline phase and the hollow dots (o) indicate the wurtzite-like ZnO crystalline phase (PDF #80-0074).

32–37° and 53–60°, four peaks of weak intensity are attributed to an early formation of crystalline zinc oxide. After thermal treatment at 200°C for 2 h, the XRD pattern of the same sample shows a completely different feature (blue line); the peaks attributed to the film precursors are no longer visible and the diffractogram is almost flat up to 40°. From 40 to 95° there are five main peaks (44.0, 50.7, 74.8, 82.0 and 91.0°) which do not correspond to a zinc oxide phase previously reported and appear of difficult attribution. In fact, the sequence of main peaks (except for that at 82.0° in 2θ) could be indexed according to a face-centred cubic (f.c.c.) sequence, suggesting the possible existence of a cubic ZnO-type phase with lattice parameter a = 3.60 Å. However, looking into the fine structure of the peaks, in particular the envelope around 44.0°, further details are visible, suggesting that the crystalline structure is not a single phase and an intermediate crystalline phase could be present (Fig. S3 of the supporting information). In sol–gel-based films, the crystallization is strongly affected by the typical anisotropic shrinkage produced during the film drying (Keddie *et al.*, 1994; Innocenzi *et al.*, 2010*c*) and, upon thermal treatment, new intermediate phases could appear. These phases are likely stabilized by the peculiar strain conditions produced in the film and the presence of organic ligands in the matrix. On the other hand, the peaks identified in the pattern of Fig. 5(*a*) (blue line) cannot be attributed to the formation of crystalline chelates or complexes made by Zn^{2+} cations with ethyl acetoacetate or acetate anions. Zn ethyl acetoacetate chelate, in fact, decomposes between 145 and 150°C (Backus & Louis, 1969) while Zn acetates, both in hydrated and dehydrated form (PDF #090676 and PDF #21-1467), show completely different X-ray patterns that do not match the experimental evidence.

At temperatures higher than 200°C (red line), the fingerprint of the X-ray diffraction pattern has almost completely changed and two main broad peaks at 34.2 and 55.6° can be observed. The peak intensity increases with thermal treatment; at 300°C the sample diffractogram shows more defined peaks that are compatible with a crystalline ZnO phase, wurtzite-like, with hexagonal structure.

The transitions of the crystalline phases with the increase of heating temperature appear more defined in the samples previously exposed to hard X-rays by DXRL. In fact, the XRD pattern of an as-deposited film exposed to a dose of 45 J cm^{-2} (Fig. 5*b*, green line) reveals the presence of strong peaks, compatible with a ZnO crystalline phase, hereafter indicated as ZnO*, with undefined crystalline structure and lattice parameter (PDF #21-1486). The same crystal structure has been recently identified in hollow zinc oxide spheres obtained at room temperature through liquid synthesis, suggesting that processing at low temperature favours the organization of ZnO crystals in that structure. (Fang *et al.*, 2014). The ZnO* formation cannot be attributed to an eventual thermal heating occurring during hard X-ray exposure because the DXRL apparatus is equipped with a water-cooling system. A similar crystalline structure could also be present in the as-deposited and not-exposed sample; however, the attribution is unclear because of the superimposition of many diffraction peaks due to the sol precursors. By comparing the patterns of X-ray-exposed films with that of a not-exposed film, we hypothesize that hard X-rays trigger the ZnO crystal growth at room temperature. After film treatment at 200°C, the XRD analysis shows the formation of a new intermediate crystalline phase, similar to what we have observed in the not-exposed films. The effect of X-ray dose, however, influences the formation of the wurtzite-like final structure, producing more defined peaks after treatment at 300°C. This trend is further confirmed by considering the thermal transition occurring in the film exposed to 178 J cm^{-2} before heat treatment (Fig. 5*c*). After heating at 250°C, in fact, the main peaks of wurtzite-like structure (PDF #80-0074) appear, indicating a hexagonal crystalline phase with lattice parameters a = 3.25 Å, c = 5.21 Å. The crystal size of the wurtzite-like ZnO, however, is very small, around 5 nm as calculated by Rietveld refinement, and it grows slightly up to 8 nm after heating at 300°C.

Interestingly, the samples exposed at doses higher or equal to 356 J cm^{-2} and treated at increasing temperatures (Fig. 5*d*)

show a direct transition from the ZnO* crystalline phase to the wurtzite-like phase without producing the unknown intermediate f.c.c. phase observed in the previous samples. The diffraction patterns allow for an estimation of the crystallite size using Rietveld refinement; the crystal dimension is 10 nm at 200°C, increases to 14 nm at 250°C and finally reaches 15.5 nm after treatment at 300°C. Once a particular ZnO crystalline phase has been obtained by thermal treatment and/or X-ray exposure, it appears stable with time and it does not undergo further modification if the films are kept at room pressure and temperature.

Fig. 6 resumes the phase transitions observed by XRD analysis as a function of the X-ray dose and the heating temperature. Immediately after deposition, the samples contain small crystallites with not well defined structure; however, hard X-rays can promote further crystallization by removing the organic compounds which are still present in the not-annealed films, allowing for the identification of the ZnO* crystalline phase (PDF #21-1486). When a thermal treatment at 250°C is applied, the crystalline phase is converted into a f.c.c. ZnO structure which is intermediate to the formation of hexagonal wurtzite-like ZnO. A direct transition from ZnO* to wurtzite-like ZnO is also possible when the film is exposed to X-ray doses higher than 178 J cm^{-2}.

The presence of the block copolymers appears to be controlling the crystallization process of zinc oxide, enabling the stabilization of new intermediate phases which have not been previously observed. At room temperature, the organic compounds inhibit the formation of crystalline ZnO*; in fact, the appearance of a definite crystalline diffraction pattern can be detected only after exposure to X-rays. Low doses, however, are not sufficient to degrade a significant amount of Pluronic and the organic compounds is still affecting the crystallization processes triggered by thermal heating at 200°C, producing the f.c.c. intermediate phase. At that temperature, in fact, the block-copolymer is not completely removed from the matrix and the ZnO crystal growth could be limited by nano-confinement. On the contrary, if the X-ray exposure dose is sufficient, a large amount of block-copolymer is removed from the matrix before thermal treatment allowing for a straight transition from ZnO* to wurtzite-like structure.

It is important to point out that, in this system, the ZnO* phase (PDF #21-1286) can be obtained only by X-ray exposure. Furthermore, only the combined use of DXRL and thermal treatment unlocks the complete control of the crystalline structure through processing and allows one of the three different crystalline phases that have been identified in the films to be selected.

The use of a templating agent also allows for an easy patterning-process of the films by DXRL. To reach microfabrication, the films immediately after deposition have been exposed to hard X-rays through a lithographic test mask using the increasing doses (Fig. 7*a*). Even at the lowest dose, the X-ray exposure causes a selective crystallization of the irradiated regions (see above) and removes a large amount of surfactant so that the films can be developed after lithography through immersion in a mixture of ethylene glycol and ethanol for 20 s. The solvents dissolve selectively the not-exposed regions of the films while the exposed parts remain on the substrate (Fig. 7*b*). The pattern quality has been evaluated by optical microscopy and X-ray micro-fluorescence (XRF); Figs 7(*c*) and 7(*d*) show a representative pattern obtained, after development, with an exposure dose of 356 J cm^{-2}; hexagonal pillars with a size of less than 100 µm have been fabricated. The pillars are well defined and no evidence of ZnO has been detected around the patterned areas, both with optical microscopy and with XRF. After thermal treatments at 300°C, the patterns shrink from an initial thickness of 480 nm

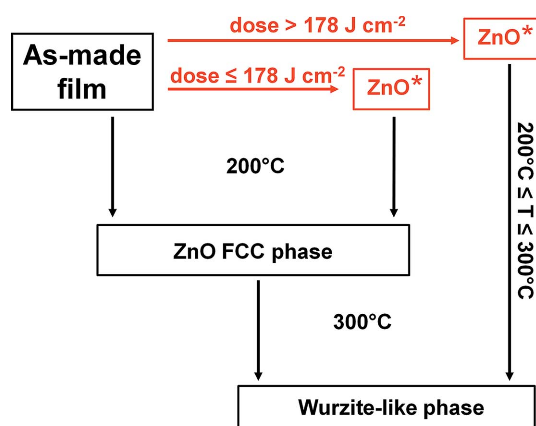

Figure 6
Phase transitions observed by XRD analysis as a function of the X-ray dose and heating temperature.

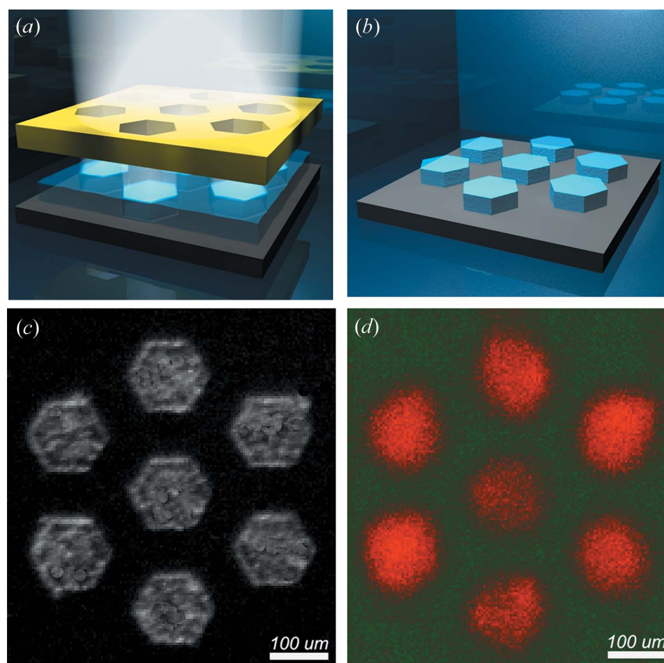

Figure 7
Schematic of the DXRL process; at first the film is exposed to hard X-rays (*a*) then the not-exposed regions are removed from the substrate through development (*b*). (*c*) Optical microscope image and (*d*) X-ray fluorescence map obtained from the integration of the Zn signal on a ZnO film after patterning with a 356 J cm^{-2} X-ray dose and development.

down to 147 nm; however, they maintain the shape induced by DXRL (Fig. S4).

4. Conclusions

A combined top-down and bottom-up approach has proven to be an effective tool towards the synthesis of Zn oxide micropatterns. The careful design of the sol enables the formation of films which are, immediately after deposition, sensitive to hard X-rays. The films, therefore, can be microfabricated through deep X-ray lithography. Besides patterning, the combined use of Pluronic F127 in the sol and X-ray exposure after film deposition has allowed tuning the crystal transition of the ZnO matrix. At low temperatures, the X-ray degradation of the block-copolymer triggers the formation of a ZnO* (PDF #21-1486) crystalline phase. On the other hand, using a thermal treatment at 200°C, we observe the formation of an intermediate f.c.c. crystalline phase which is correlated with the presence of a residual organic compound in the matrix. In fact, when higher exposure doses are applied to the films before heating, the ZnO shows a direct transition from ZnO* to wurtzite-like (PDF #80-0074) structure, in accordance with previous findings (Fang *et al.*, 2014). Despite some previous papers reporting on the synthesis of the ZnO* and/or wurzite-like phase, the full integration of bottom-up synthesis and top-down lithography allows a double degree of control in the matrix to be obtained; we can, in fact, select a specific crystalline phase of zinc oxide, through a combined use of thermal treatment and X-rays dose, and produce precise patterning through deep X-ray lithography. After X-ray exposure, in fact, the samples can be developed under mild conditions by using a solution of ethanol and ethylene glycol. The process is fast, efficient and produces sharp features of the patterns; no residues have been detected in the not-exposed areas, as revealed by X-ray microfluorescence. The combined approach we have proposed opens new perspectives in the patterning and simultaneous physico-chemical tuning of polymorphic oxide coatings deposited by the liquid phase.

PF acknowledges the ARC for support (DE120102451). D. Carboni and C. D. Lancillotto are acknowledged for their support.

References

Backus, A. C. & Louis, L. L. (1969). US Patent 3 453 300.
Cho, K. W., Yi, S. H., Son, Y. H. & Kweon, S. Y. (2007). *Integr. Ferroelectr.* **89**, 141–149.
Costacurta, S., Falcaro, P., Malfatti, L., Marongiu, D., Marmiroli, B., Cacho-Nerin, F., Amenitsch, H., Kirkby, N. & Innocenzi, P. (2011). *Langmuir*, **27**, 3898–3905.
Cuscó, R., Alarcón-Lladó, E., Ibáñez, J., Artús, L., Jiménez, J., Wang, B. & Callahan, M. J. (2007). *Phys. Rev. B*, **75**, 165202–1–11.
Falcaro, P., Costacurta, S., Malfatti, L., Takahashi, M., Kidchob, T., Casula, M. F., Piccinini, M., Marcelli, A., Marmiroli, B., Amenitsch, H., Schiavuta, P. & Innocenzi, P. (2008). *Adv. Mater.* **20**, 1864–1869.
Falcaro, P., Malfatti, L., Vaccari, L., Amenitsch, H., Marmiroli, B., Grenci, G. & Innocenzi, P. (2009). *Adv. Mater.* **21**, 4932–4936.
Fang, L., Zhang, B., Li, W., Li, X., Xin, T. & Zhang, Q. (2014). *RSC Adv.* **4**, 7167–7173.
Farley, N. R. S., Staddon, C. R., Zhao, L. X., Edmonds, K. W., Gallagher, B. L. & Gregory, D. H. (2004). *J. Mater. Chem.* **14**, 1087–1092.
Guo, L., Ji, Y., Xu, H., Wu, Z. & Simon, P. (2003). *J. Mater. Chem.* **13**, 754–757.
Hu, W., Liu, Y., Yang, H., Zhou, X. & Li, C. M. (2011). *Biosens. Bioelectron.* **26**, 3683–3687.
Innocenzi, P., Kidchob, T., Costacurta, S., Falcaro, P., Marmiroli, B., Cacho-Nerin, F. & Amenitsch, H. (2010*a*). *Soft Matter*, **6**, 3172–3176.
Innocenzi, P., Malfatti, L. & Falcaro, P. (2012). *Soft Matter*, **8**, 3722–3729.
Innocenzi, P., Malfatti, L., Kidchob, T., Costacurta, S., Falcaro, P., Marmiroli, B., Cacho-Nerin, F. & Amenitsch, H. (2011). *J. Synchrotron Rad.* **18**, 280–286.
Innocenzi, P., Malfatti, L., Kidchob, T., Enzo, S., Ventura, G. D., Schade, U. & Marcelli, A. (2010*c*). *J. Phys. Chem. C*, **114**, 22385–22391.
Innocenzi, P., Malfatti, L., Marmiroli, B. & Falcaro, P. (2004). *J. Sol-Gel Sci. Technol.* **70**, 236–244.
Innocenzi, P., Malfatti, L., Piccinini, M. & Marcelli, A. (2010*b*). *J. Phys. Chem. A*, **114**, 304–308.
Keddie, J. L., Braun, P. V. & Giannelis, E. P. (1994). *J. Am. Ceram. Soc.* **77**, 1592–1596.
Krunks, M. & Mellikov, E. (1995). *Thin Solid Films*, **270**, 33–36.
Lee, J. S., Oh, M. H., Kumar, P., Khanna, A., Singh, R. K. & Ranade, M. B. (2011). *J. Therm. Spray Tech.*, **20**, 1001–1008.
Lutterotti, L., Matthies, S. & Wenk, H.-R. (1999). *IUCr Newsl.* **21**, 14–15.
Malfatti, L., Falcaro, P., Marmiroli, B., Amenitsch, H., Piccinini, M., Falqui, A. & Innocenzi, P. (2011). *Nanoscale*, **3**, 3760–3766.
Malfatti, L., Marongiu, D., Costacurta, S., Falcaro, P., Amenitsch, H., Marmiroli, B., Grenci, G., Casula, M. F. & Innocenzi, P. (2010). *Chem. Mater.* **22**, 2132–2137.
Mandalapu, L. J., Xiu, F. X., Yang, Z., Zhao, D. T. & Liu, J. L. (2006). *Appl. Phys. Lett.* **88**, 112108.
Mikó, A., Demirel, A. L. & Somer, M. (2012). *J. Mater. Chem.* **22**, 3705–3707.
Naghavi, N., Marcel, C., Dupont, L., Rougier, A., Leriche, J. B. & Guéry, C. (2000). *J. Mater. Chem.* **10**, 2315–2319.
Natsume, Y. & Sakata, H. (2002). *Mater. Chem. Phys.* **78**, 170–176.
O'Brien, S., Nolan, M. G., Çopuroglu, M., Hamilton, J. A., Povey, I., Pereira, L., Martins, R., Fortunato, E. & Pemble, M. (2010). *Thin Solid Films*, **518**, 4515–4519.
Özgür, Ü., Alivov, Y. I., Liu, C., Teke, A., Reshchikov, M. A., Doğan, S., Avrutin, V., Cho, S. J. & Morkoç, H. (2005). *J. Appl. Phys.* **98**, 041301.
Pinna, A., Lasio, B., Piccinini, M., Marmiroli, B., Amenitsch, H., Falcaro, P., Tokudome, Y., Malfatti, L. & Innocenzi, P. (2013). *Appl. Mater. Interfaces*, **5**, 3168–3175.
Pinna, A., Malfatti, L., Piccinini, M., Falcaro, P. & Innocenzi, P. (2012). *J. Synchrotron Rad.* **19**, 586–590.
Seisenbaeva, G. A. & Kessler, V. G. (2014). *Nanoscale*, **6**, 6229–6244.
Tominaga, K., Takao, T., Fukushima, A., Moriga, T. & Nakabayashi, I. (2002). *Vacuum*, **66**, 505–509.